

# Elastic Properties and Fracture Behaviors of Biaxially Deformed, Polymorphic MoTe<sub>2</sub>

Yufei Sun,<sup>†,@</sup> Jinbo Pan,<sup>∇,@</sup> Zetao Zhang,<sup>‡,@</sup> Kenan Zhang,<sup>‡</sup> Jing Liang,<sup>○</sup> Weijun Wang,<sup>◆</sup> Zhiquan Yuan,<sup>†</sup> Yukun Hao,<sup>||</sup> Bolun Wang,<sup>†</sup> Jingwei Wang,<sup>◆</sup> Yang Wu,<sup>§</sup> Jingying Zheng,<sup>⊥</sup> Liying Jiao,<sup>⊥</sup> Shuyun Zhou,<sup>‡,||</sup> Kaihui Liu,<sup>○</sup> Chun Cheng,<sup>◆</sup> Wenhui Duan,<sup>‡,||,#</sup> Yong Xu,<sup>\*,‡,||,∅</sup> Qimin Yan,<sup>\*,∇</sup> and Kai Liu<sup>\*,†,◆</sup>

<sup>†</sup>State Key Laboratory of New Ceramics and Fine Processing, School of Materials Science and Engineering, <sup>‡</sup>State Key Laboratory of Low-Dimensional Quantum Physics, Department of Physics, <sup>§</sup>Tsinghua-Foxconn Nanotechnology Research Center, <sup>||</sup>Center for Nano- and Micro-Mechanics, <sup>⊥</sup>Key Laboratory of Organic Optoelectronics and Molecular Engineering of the Ministry of Education, Department of Chemistry, and <sup>#</sup>Institute for Advanced Study, Tsinghua University, Beijing 100084, China

<sup>∇</sup>Department of Physics, Temple University, Philadelphia, Pennsylvania 19122, United States

<sup>○</sup>School of Physics, Academy for Advanced Interdisciplinary Studies, Peking University, Beijing 100871, China

<sup>◆</sup>Department of Materials Science and Engineering, Southern University of Science and Technology, Shenzhen 518055, China

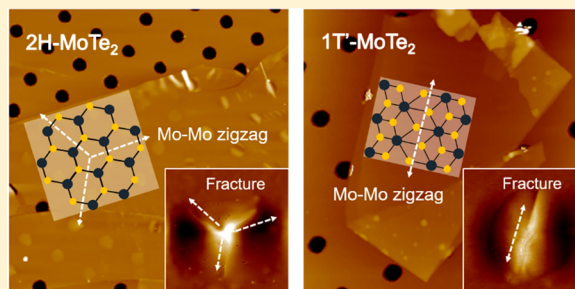
<sup>||</sup>Collaborative Innovation Center of Quantum Matter, Beijing 100084, China

<sup>∅</sup>RIKEN Center for Emergent Matter Science (CEMS), Wako, Saitama 351-0198, Japan

## Supporting Information

**ABSTRACT:** Biaxial deformation of suspended membranes widely exists and is used in nanoindentation to probe elastic properties of structurally isotropic two-dimensional (2D) materials. However, the elastic properties and, in particular, the fracture behaviors of anisotropic 2D materials remain largely unclarified in the case of biaxial deformation. MoTe<sub>2</sub> is a polymorphic 2D material with both isotropic (2H) and anisotropic (1T' and T<sub>d</sub>) phases and, therefore, an ideal system of single-stoichiometric materials with which to study these critical issues. Here, we report the elastic properties and fracture behaviors of biaxially deformed, polymorphic MoTe<sub>2</sub> by combining temperature-variant nanoindentation and first-principles calculations. It is found that due to similar atomic bonding, the effective moduli of the three phases deviate by less than 15%. However, the breaking strengths of distorted 1T' and T<sub>d</sub> phases are only half the value of 2H phase due to their uneven distribution of bonding strengths. Fractures of both isotropic 2H and anisotropic 1T' phases obey the theorem of minimum energy, forming triangular and linear fracture patterns, respectively, along the orientations parallel to Mo–Mo zigzag chains. Our findings not only provide a reference database for the elastic behaviors of versatile MoTe<sub>2</sub> phases but also illuminate a general strategy for the mechanical investigation of any isotropic and anisotropic 2D materials.

**KEYWORDS:** MoTe<sub>2</sub>, elastic properties, phase transition, nanoindentation



Elastic properties are key determinants for the strain engineering of two-dimensional (2D) materials<sup>1–4</sup> and also play vital roles in the designs of flexible 2D devices. 2D materials have been reported to have ultrahigh in-plane modulus ( $E^{2D}$ ) and breaking strength ( $\sigma_0^{2D}$ ) in contrast to their 3D counterparts.<sup>5–7</sup> Their superior stiffness and flexibility have enabled lots of functions in flexible transistors, resonators, and oscillators.<sup>8,9</sup> Experimentally, elastic properties of 2D materials can be facily probed by nanoindentation under atomic force microscopy (AFM), in which a suspended, circular membrane of a 2D material is imposed with a biaxial strain by indenting the center with an AFM tip.<sup>5,10</sup> The nanoindentation of circular membranes is a reliable way to investigate the elastic properties and fracture behaviors of

ultrathin materials because it avoids both the non-uniformity of strain and the defect-initiated breaking from edges that usually occur in the approach of the uniaxial stretch of thin films. Therefore, nanoindentation has been intensively used to investigate structurally isotropic 2D materials such as graphene and 2H-MoS<sub>2</sub>.<sup>5–7,11</sup> For the investigation of anisotropic 2D materials, however, uniaxial stretch is still considered to be necessary, and thereby, ribbon-like materials or trenches are defined by complicated, multistep microfabrication.<sup>12</sup> Although several anisotropic 2D materials have been

**Received:** September 21, 2018

**Revised:** January 5, 2019

**Published:** January 9, 2019

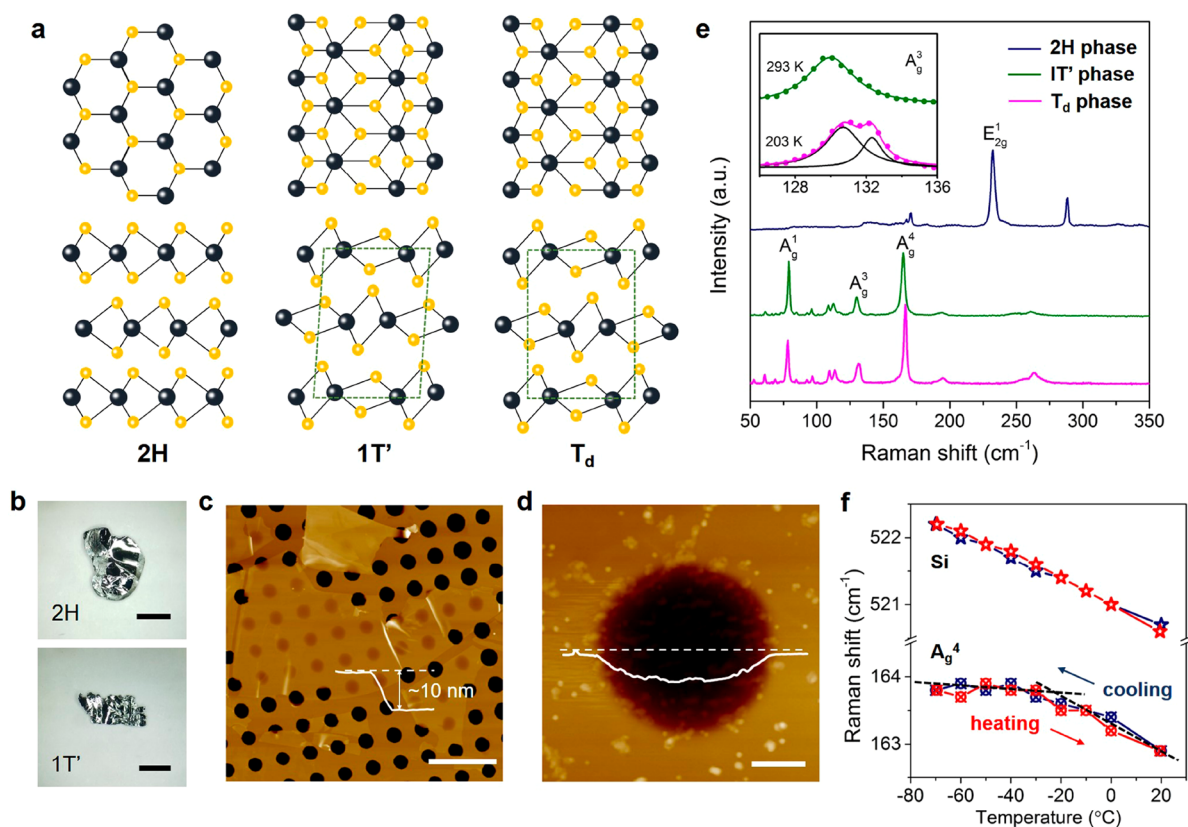


**Figure 1.** Crystalline structures and characterizations of the three MoTe<sub>2</sub> phases. (a) Illustration of crystalline structures of 2H-, 1T'-, and T<sub>d</sub>-MoTe<sub>2</sub>. (b) Bulk crystals of 2H- and 1T'-MoTe<sub>2</sub> used in this work. (c) AFM topography of a 1T'-MoTe<sub>2</sub> sample  $\sim$ 10 nm thick over a holey substrate. (d) Surface morphology of MoTe<sub>2</sub> over a single hole. The white line in panel d is the height scan of the sample following the dashed line. (e) Raman spectra of the three phases. The T<sub>d</sub> phase was measured at 203 K, and the A<sub>g</sub><sup>3</sup> peak splits into two peaks, as enlarged in the inset. (f) Temperature dependence of the Raman shifts of A<sub>g</sub><sup>4</sup> peak (MoTe<sub>2</sub>) and Si peak during heating and cooling. The slope of the A<sub>g</sub><sup>4</sup> curve changes at  $\sim$ 250 K, where a phase transition occurs. Scale bars: (b) 2 mm, (c) 5  $\mu$ m, and (d) 400 nm.

investigated by nanoindentation recently, their elastic properties and particularly fracture behaviors in the case of biaxial deformation have yet to be clarified.<sup>13</sup>

The two-dimensional transition metal dichalcogenides (TMDCs) attract great interests in recent years because of their extraordinary and tunable properties by temperature, strain, doping, phase transition, and van der Waals (vdW) stacking. This has made 2D TMDCs prospective materials for applications in electronics, photonics, spintronics, and electro-mechanics.<sup>8,9,14–18</sup> MoTe<sub>2</sub> is a typical yet unique TMDC with both structurally isotropic (hexagonal 2H) and anisotropic (distorted octahedral 1T' and octahedral T<sub>d</sub>) phases around room temperature (Figure 1a). The three phases have shown remarkably different electrical transport properties. The 2H-MoTe<sub>2</sub> is semiconducting with a bandgap of  $\sim$ 1 eV. The 1T' phase is metallic, and its monolayer is predicted to be a 2D topological insulator. The T<sub>d</sub> phase has been recently recognized as a type II Weyl semimetal that exhibits novel quantum phenomena.<sup>14,19–23</sup> The 2H-to-1T' transition could be triggered by temperature, laser irradiation, or electrostatic doping, while the 1T'-to-T<sub>d</sub> transition occurs at  $\sim$ 250 K at atmospheric pressure.<sup>20,22,24</sup> The versatile phases thus have made MoTe<sub>2</sub> a perfect group of materials with single stoichiometry for the clarification of elastic properties and fracture behaviors of both isotropic and anisotropic 2D structures.

In this work, we studied the elastic properties and fracture behaviors of 2H-, 1T'- and T<sub>d</sub>-MoTe<sub>2</sub> by means of temper-

ature-variant, biaxially deformed nanoindentation and first-principles calculations. The effective  $E^{2D}$  of the three phases are found to be similar to minor deviations of less than 15%, but their breaking strengths show large diversities. Density functional theory (DFT) calculations show consistent  $E^{2D}$  values for the three phases, and we attribute the lower strengths in the 1T' and T<sub>d</sub> phases to their uneven distribution of bonding strengths due to their distorted structures. We also clearly observe that there exists a triangular-shape fracture pattern in the 2H phase and linearly shaped or T-shape patterns in the 1T' phase. Polarization-resolved second harmonic generation (SHG) experiments prove that the fracture patterns propagate along the Mo–Mo zigzag directions in both isotropic and anisotropic phases, which obeys the theorem of minimum energy as revealed by the DFT calculations. Both the elastic properties and the fracture behaviors of the three phases are found to depend on their structural symmetry, which also suggests that the facile nanoindentation providing with biaxial deformation is capable of probing both isotropic and anisotropic 2D materials.

The samples of 2H- and 1T'-MoTe<sub>2</sub> thin flakes were prepared by mechanical exfoliation from bulk crystals (Figure 1b) onto a SiO<sub>2</sub> (285 nm thick)/Si substrate, which was pre-patterned with arrays of circular holes that are  $\sim$ 1  $\mu$ m in diameter and 285 nm in depth. The samples of T<sub>d</sub> phase were obtained by cooling the 1T' samples to below 250 K. The surface topography and the thicknesses of the membranes were characterized by AFM (Figures 1c,d and S1). Transmission

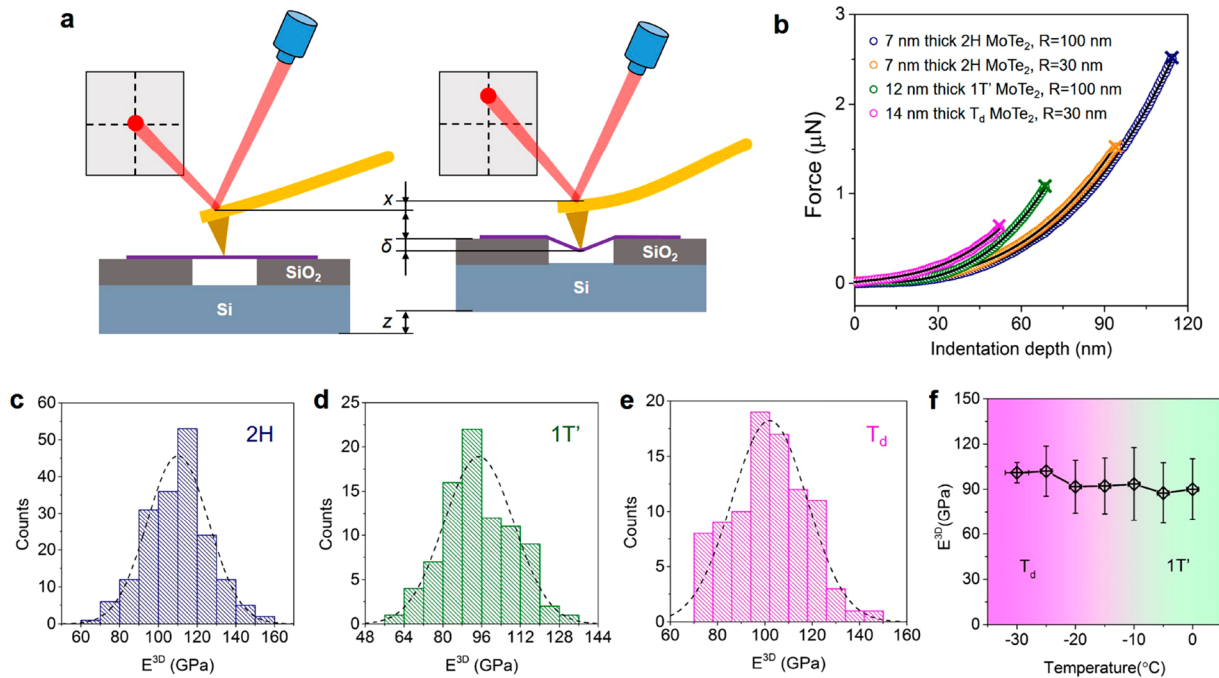


**Figure 2.** Nanoindentation experiments for the three MoTe<sub>2</sub> phases. (a) Schematic diagram of the nanoindentation process. The indentation depth  $\delta$  is determined by  $\delta = z - x$ , where  $z$  is the moving distance of the sample stage that is controlled by the piezoelectric scanner and  $x$  is the deflection of the AFM probe detected by a laser reflection system. (b) Dependence of indentation force on indentation depth for the three MoTe<sub>2</sub> phases, which was measured by two tips with different diameters. The cross marks at the end of each curve indicate the fracture points of the membranes. (c–e) Histograms of elastic moduli of 2H-, 1T', and T<sub>d</sub>-MoTe<sub>2</sub>, respectively. (f) Elastic moduli of a 1T' sample measured by temperature-variant nanoindentation across its 1T'-to-T<sub>d</sub> phase transition.

electron microscopy (TEM) analysis indicates that the samples are single crystals without microcracks or flaws (Figure S2). Figure 1e shows the Raman spectra of the three phases. For 1T' and T<sub>d</sub> phases, the Raman spectra are almost identical because of their similar crystal structures except the A<sub>g</sub><sup>3</sup> peak at 128~134 cm<sup>-1</sup>, which splits into two peaks, namely A<sub>g</sub><sup>3</sup> and A<sub>g</sub><sup>3'</sup>, across the transition from 1T' to T<sub>d</sub> phase. The latter peak originates from the out-of-plane vibration mode and cannot be detected in the 1T' phase because of the existence of inversion symmetry.<sup>25,26</sup> Temperature-variant Raman spectra were also conducted to further understand the 1T'-to-T<sub>d</sub> phase transition. Figures 1f and S3 show a blue shift of A<sub>g</sub><sup>3</sup> peak of 1T'-MoTe<sub>2</sub> when cooling the sample. It has an evident slope change at the temperature around 250 K, indicating the 1T'-to-T<sub>d</sub> transition, which is consistent with the previous results probed by electrical measurements.<sup>19,21</sup> As a comparison, the Raman peak of Si without any phase transitions at this temperature range shows an almost linear increase during the cooling, also consistent with literature.<sup>27</sup>

Prior to the nanoindentation test, the sample was scanned in tapping-mode AFM for a few times until its thermal drift is not noticeable. Then, the AFM tip was positioned at the center of a hole covered by a suspended MoTe<sub>2</sub> membrane. With the sample stage moving upward, a point load was applied onto the center of the suspended membrane to deform it biaxially by the AFM tip (Figure 2a). The indentation depth  $\delta$  is defined as the displacement of the center of the suspended membrane. The applied force  $F$  can be calculated by Hooke's law,  $F = kx$ , where  $k$  is the spring constant of the AFM probe that is calibrated by the Sader method (see Figure S4). In our experiments, because the membranes measured are 3–14 nm in thickness and the contribution of out-of-plane shearing stress is negligible, the

nonlinear-membrane model applies according to our calculations (Figure S5)<sup>7,10</sup> following the equation:<sup>5,10,28</sup>

$$F = \left[ E^{2D} \frac{4\pi t^2}{3r^2(1-\nu^2)} \right] \delta + (\sigma^{2D} \pi) \delta + \left( E^{2D} \frac{q^3}{r^2} \right) \delta^3 \quad (1)$$

where  $E^{2D}$  is the in-plane elastic modulus,  $\sigma^{2D}$  is the pretension of the suspended membrane over a hole,  $t$  is the thickness of the membrane,  $r$  is the radius of the hole, and  $q = 1/(1.05 - 0.15\nu - 0.16\nu^2)$  is a factor determined by the Poisson's ratio  $\nu$ . The first term in eq 1 corresponds to the bending behavior of the membrane with a bending rigidity  $D = E^{2D}t^2/12(1-\nu^2)$ . The second and the third terms are related to the contributions from pretension ( $\sigma^{2D}$ ) and elastic deformation ( $E^{2D}$ ), respectively. Here, we take  $q = 1.00$  for the 2H phase and  $q = 1.02$  for the 1T' and T<sub>d</sub> phases according to the theoretical results from first-principles calculations that will be discussed later.

As is also deduced from eq 1, the  $F$ - $\delta$  curve appears linear when the indentation depth  $\delta$  is small. With the increase of the indentation depth  $\delta$ , the in-plane elastic deformation becomes dominant, and  $F$  is finally ruled by a cubic order of  $\delta$  (Figure S6). When the force finally reaches the breaking point, the suspended membrane collapses, and its breaking strength could be thus measured following the equation:

$$\sigma_0^{2D} = \left( \frac{F_0 E^{2D}}{4\pi R} \right)^{1/2} \quad (2)$$

where  $F_0$  is the fracture force and  $R$  is the radius of the AFM tip. In our experiments,  $R$  was measured through scanning electron microscopy (SEM) (Figure S7).

Eqs 1 and 2 have well described the elastic behaviors of structurally isotropic 2D materials. For anisotropic 2D materials, the indentation of a circular membrane will introduce an identical strain but different stresses along different lattice directions due to the anisotropy in modulus. To describe the elastic response of an anisotropic 2D material under tension, we introduce an equivalent elastic modulus ( $E_{\text{eq}}$ ). Continuum mechanics theory has shown that  $E_{\text{eq}}$  is a function of the elastic modulus ( $E_x, E_y$ ), in-plane shearing modulus ( $G$ ), and the Poisson's ratio ( $\nu_x, \nu_y$ ) (see the Supporting Information S11 for details) following:

$$E_{\text{eq}} = \frac{3}{8}(E_x + E_y) + \frac{1}{8}(E_x\nu_x + E_y\nu_y) + \frac{G}{2}(1 - \nu_x\nu_y) \quad (3)$$

The theoretical  $E_{\text{eq}}$  is expected to be identical to the value of experimental  $E^{2\text{D}}$ . With the  $E_{\text{eq}}$ , the equivalent breaking strength of an isotropic 2D material should also follow the eq 2 and is determined by the lattice orientation that can sustain the minimum strain upon breaking.

We conducted the nanoindentation experiments on 23 circular membranes in 3 flakes of 2H-MoTe<sub>2</sub>, 12 membranes in 2 flakes of 1T'-MoTe<sub>2</sub>, and 14 membranes in 3 flakes of T<sub>d</sub>-MoTe<sub>2</sub>. Each circular membrane was indented with at least 5 different applied forces before its fracture. The T<sub>d</sub> phase was probed by cooling down the 1T' phase sample from room temperature to 243~245 K with a cryostat (Multimode cooler) under the AFM.

Previous studies including ours have shown that the interlayer sliding will soften the modulus of a layered material.<sup>6</sup> As a result, if there exists an interlayer sliding, the measured  $E^{3\text{D}}$  would gradually decrease with the increase of the membrane thickness. Whether an interlayer sliding will occur depends on the strength of vdW interlayer interaction and the strain applied on the material. It has been reported that in black phosphorus,  $E^{3\text{D}}$  decreases with increasing the number of layers,<sup>29</sup> but in WSe<sub>2</sub>,  $E^{3\text{D}}$  is independent of it.<sup>13</sup> In our experiment, we found that  $E^{2\text{D}}$  shows a good linear relationship with the membrane thickness, and thus,  $E^{3\text{D}}$  generally remains unchanged (see Figure S8). This result suggests that the interlayer sliding of MoTe<sub>2</sub> is negligible in our experimental conditions. The force induced by compressing the gas in the sealed hole is also calculated, and its impact is found to be negligible (see the Supporting Information for detailed discussion). These results have indicated that our experiment fits well with the mechanical model, and that the mechanical properties of the multilayer samples can be extended to apply on monolayer ones. Typical force-indentation depth ( $F-\delta$ ) curves are shown in Figure 2b. The coefficients of determination (R-square) for most force curves are larger than 0.999, indicating a good fitting of the data.

The 2D elastic modulus relates to the change of planar elastic energy upon deformation, which has a unit of joules per square meter or newtons per meter. By dividing the 2D modulus by the sample thickness measured by the AFM, we get the 3D modulus with a unit of N/m<sup>2</sup> or Pa. This conversion provides an approach to comparing the stiffness of thin 2D materials with the values of bulk materials. Table 1 shows the data related to the measurements for the three phases. The  $E^{3\text{D}}$  are calculated as  $110 \pm 16$  GPa for 2H-MoTe<sub>2</sub>,  $99 \pm 15$  GPa for 1T'-MoTe<sub>2</sub>, and  $102 \pm 16$  GPa for T<sub>d</sub>-MoTe<sub>2</sub>, all of which are of small deviations (<15%) and about 40% the modulus of MoS<sub>2</sub> (~270 GPa).<sup>7</sup> Figure 2c-e

**Table 1. Elastic Properties of the Three Phases in Different Samples<sup>a</sup>**

phase	sample no.	thickness (nm)	$E^{2\text{D}}$ (N/m)	$\sigma_0^{2\text{D}}$ (N/m)	$\sigma_0^{2\text{D}}/E^{2\text{D}}$ (%)	$E^{3\text{D}}$ (GPa)	$\sigma_0^{3\text{D}}$ (GPa)
2H	1	3.6	316	26.1	8.3	87.8	7.3
	2	6.7	668	30.5	4.6	99.7	4.6
	3	6.0	675	42.0	6.2	112.5	7.0
1T'	1	9.0	936	24.8	2.7	104.0	2.8
	2	11.0	1073	27.6	2.6	97.6	2.5
T <sub>d</sub>	1	13.0	1318	41.7	3.2	101.4	3.2
	2	10.5	1084	33.4	3.1	103.3	3.2
	3	14.0	1218	30.5	2.5	87.0	2.2

<sup>a</sup> $E^{2\text{D}}$  and  $\sigma_0^{2\text{D}}$  are obtained by fitting measured  $F-\delta$  curves with eqs 1 and 2, respectively.  $E^{3\text{D}}$  and  $\sigma_0^{3\text{D}}$  are derived by dividing  $E^{2\text{D}}$  and  $\sigma_0^{2\text{D}}$  values by membrane thicknesses.

shows statistical diagrams of the 3D moduli of the three MoTe<sub>2</sub> phases, which fits well with Gaussian distribution and validates the reliability of our experiments. Figure 2f shows the dependence of Young's moduli of the sample on temperature. The Young's moduli increase slightly at 248 and 243 K, where the sample should have entered the T<sub>d</sub> phase. These results provide quantitative data for the evolution of MoTe<sub>2</sub> elastic properties across its 1T'-to-T<sub>d</sub> transition.

The breaking strengths ( $\sigma_0^{3\text{D}}$ ), however, differ largely for different MoTe<sub>2</sub> phases. The  $\sigma_0^{3\text{D}}$  of 1T' phase and T<sub>d</sub> phase are similar ( $2.6 \pm 0.2$  and  $2.5 \pm 0.9$  GPa, respectively) but less than half the value of 2H phase ( $5.6 \pm 1.3$  GPa). These phenomena suggest that the elastic modulus and breaking strength are affected by different physical factors. Traditional mechanic theory of materials has shown that elastic modulus is only determined by the atomic bonding. This theory is also applicable to 2D crystals because the 2D modulus reflects the change in planar elastic energy originated from the deformation of the atomic bonds. Because all phases of MoTe<sub>2</sub> share similar bonding conditions, with each Mo atom shared by six adjacent Te atoms through covalent bond, the in-plane elastic modulus is less phase-sensitive. However, the strength of a membrane is related to the minimum energy to break the atomic bonding, and therefore, the fracture is more complex and sensitive to multiple factors including bonding, crystal structure, crystal orientation, defects, etc.<sup>12,30-32</sup>

To further investigate the elastic properties of polymorphic MoTe<sub>2</sub>, geometric relaxations and strain calculations of 2H, 1T', and T<sub>d</sub> phases of MoTe<sub>2</sub> were performed using density functional theory (DFT) within projector-augmented wave (PAW) potentials<sup>33</sup> as implemented in the VASP code<sup>34,35</sup> (details of the calculations can be found in the Materials and Methods section and Figure S9). Panels a-c of Figure 3 are the contour plots of changes in elastic energy as functions of strains along armchair and zigzag directions for 2H-, 1T'- and T<sub>d</sub>-MoTe<sub>2</sub>, respectively. As can be calculated, the isotropic  $E^{3\text{D}}$  of 2H-MoTe<sub>2</sub> is 117.8 GPa, which is very close to the values reported in previous study.<sup>36</sup> The  $E^{3\text{D}}$  of 1T'-MoTe<sub>2</sub> is 124.5 GPa along armchair direction and 96.0 GPa along zigzag direction, respectively. The value of T<sub>d</sub>-MoTe<sub>2</sub> is 124.9 GPa along the armchair direction and 97.6 GPa along the zigzag direction. It is obvious that for both 1T'- and T<sub>d</sub>-MoTe<sub>2</sub>, the elastic modulus differs by approximately 25% between the two orthogonal directions. Because 1T'- and T<sub>d</sub>-MoTe<sub>2</sub> show a small difference in modulus along the two orthogonal directions, the in-plane shearing modulus  $G$  can be estimated

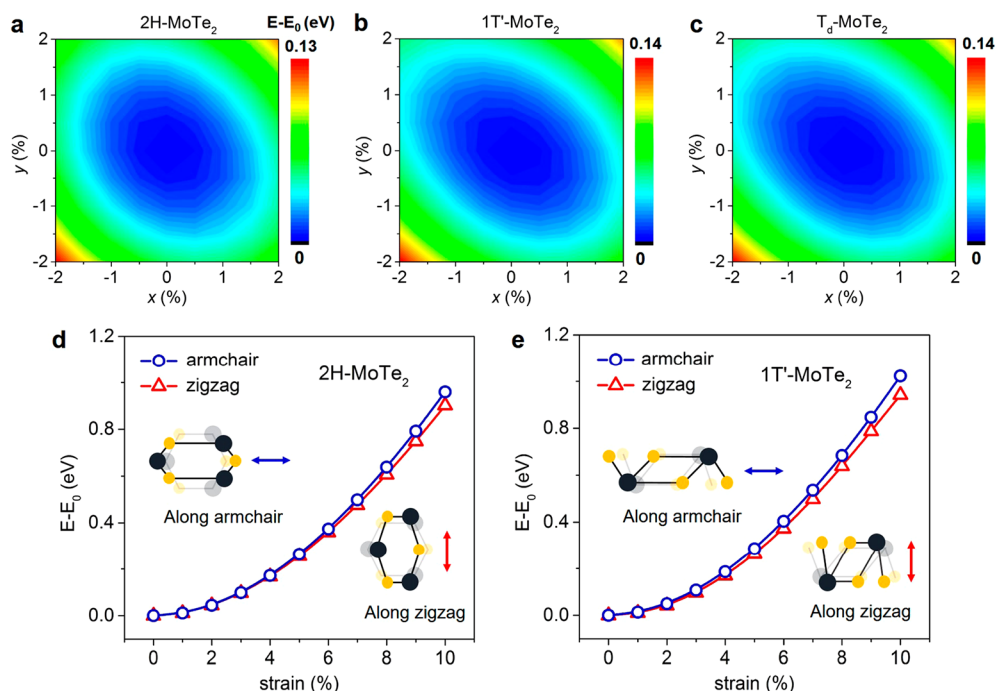


**Figure 3.** DFT calculations of elastic properties of bulk MoTe<sub>2</sub>. (a–c) Contour plot of change in elastic energy along the *x* (armchair) and *y* (zigzag) lattice directions as functions of strain for 2H-, 1T'-, and T<sub>d</sub>-MoTe<sub>2</sub>, respectively. (d, e) Dependence of elastic energy on strains along two orthogonal directions for 2H- and 1T'-MoTe<sub>2</sub>, respectively. The insets indicate deformation of unit cells along different lattice directions under a uniaxial strain.

to be a range of value by the isotopic model, where  $G = E/2(1 + \nu)$ . As such, theoretical equivalent modulus can be estimated according to eq 3 in the case of biaxial deformation to be  $110 \pm 3$  GPa for 1T'-MoTe<sub>2</sub> and  $111 \pm 3$  GPa for T<sub>d</sub>-MoTe<sub>2</sub>, both close to the experimental values. The elastic energy versus strain curves of isotropic 2H- and anisotropic 1T'-MoTe<sub>2</sub> under a uniaxial strain up to 10% are also plotted in Figure 3d,e. It reveals that the elastic energies of 2H phase are almost the same along the two orthogonal directions at a small strain (<5%) and deviate slightly with a higher value along the armchair direction when the strain further increases. For the 1T' phase, the elastic energy along the armchair direction is always larger than that along the zigzag direction under the same strain. This calculation also shows that when the strain is within the calculated range (10%), both 2H- and 1T'-MoTe<sub>2</sub> still remain elastic. Note that in experiments, the breaking strains ( $\sigma_0^{2D}/E^{2D}$ ; see Table 1) are smaller than 10%, suggesting a brittle fracture mechanism for both 2H- and 1T'-MoTe<sub>2</sub>, probably due to point defects that are unavoidably induced during the crystals growth. The fracture behavior should follow the theorem of minimum energy that will be discussed later.<sup>37</sup>

With the biaxial deformation in nanoindentation, we can also experimentally study the fracture behaviors of both isotropic 2H-MoTe<sub>2</sub> and anisotropic 1T'-MoTe<sub>2</sub>. As shown in Figure 4a, Y-shaped fractures are mostly observed among the 2H-MoTe<sub>2</sub> samples. The angles between adjacent fracture orientations are approximately 120°, revealing a 3-fold symmetry of lattice in the 2H phase. In contrast, I-shaped patterns form in most 1T'-MoTe<sub>2</sub> samples (Figure 4d), meaning that there exists a preferred fracture orientation. In some other 1T'-MoTe<sub>2</sub> samples, T-shaped patterns are observed (Figure 4e), indicating that besides the preferred I-shaped fracture, a secondary linear fracture may occur during

the nanoindentation. To experimentally determine the relationship between the preferred fracture and the lattice orientations, we conducted polarization-resolved SHG experiments on the 2H- and 1T'-MoTe<sub>2</sub> samples. Panels b and f of Figure 4 show the SHG polarization polar map of the 2H and 1T' samples, respectively, with altering the angle of the incident laser. For the hexagonal 2H phase, the SHG shows a 6-fold pattern, with the petals indicating the armchair directions. For the distorted octahedral 1T' phase, the SHG pattern is binary symmetric, and the direction of the minimum intensity (plotted with a green arrow) is parallel to the Mo–Mo zigzag alignment, as reported by the previous research.<sup>23,38</sup> These SHG results confirm the lattice directions in the 2H- and 1T'-MoTe<sub>2</sub> samples. By comparing the fracture directions (Figure 4a,d) and the lattice orientations (Figure 4b,f), we conclude that the preferred fracture orientation in both the 2H and the 1T'-MoTe<sub>2</sub> is parallel to the Mo–Mo zigzag chains, which are labeled by the blue and green arrows as a reference.

According to the theorem of minimum energy, the generation of fractures in 2D materials is determined by a competition between the cost in edge formation energy ( $\Delta E$ ) and the gain in elastic energy. The typical edge formation energy ( $\Delta E_1$ ) includes energy contributions from edge-bond breaking as well as edge-structure relaxation, which are plotted by the hollow symbols in Figure 5c,d. However, considering that the edge relaxation after the bond breaking is irrelevant to fracture behaviors in the theorem of minimum energy, one should use the edge formation energy excluding structural relaxation ( $\Delta E_2$ , solid symbols in Figure 5c,d) instead of  $\Delta E_1$  for the study of fracture, as we will demonstrate. Here, we calculated both  $\Delta E_1$  and  $\Delta E_2$  for monolayer 2H- and 1T'-MoTe<sub>2</sub> by considering nanoribbons with varying widths (see details in the Materials and Methods section). As shown by the solid symbols in Figure 5, the calculated  $\Delta E_1$  and  $\Delta E_2$  depend

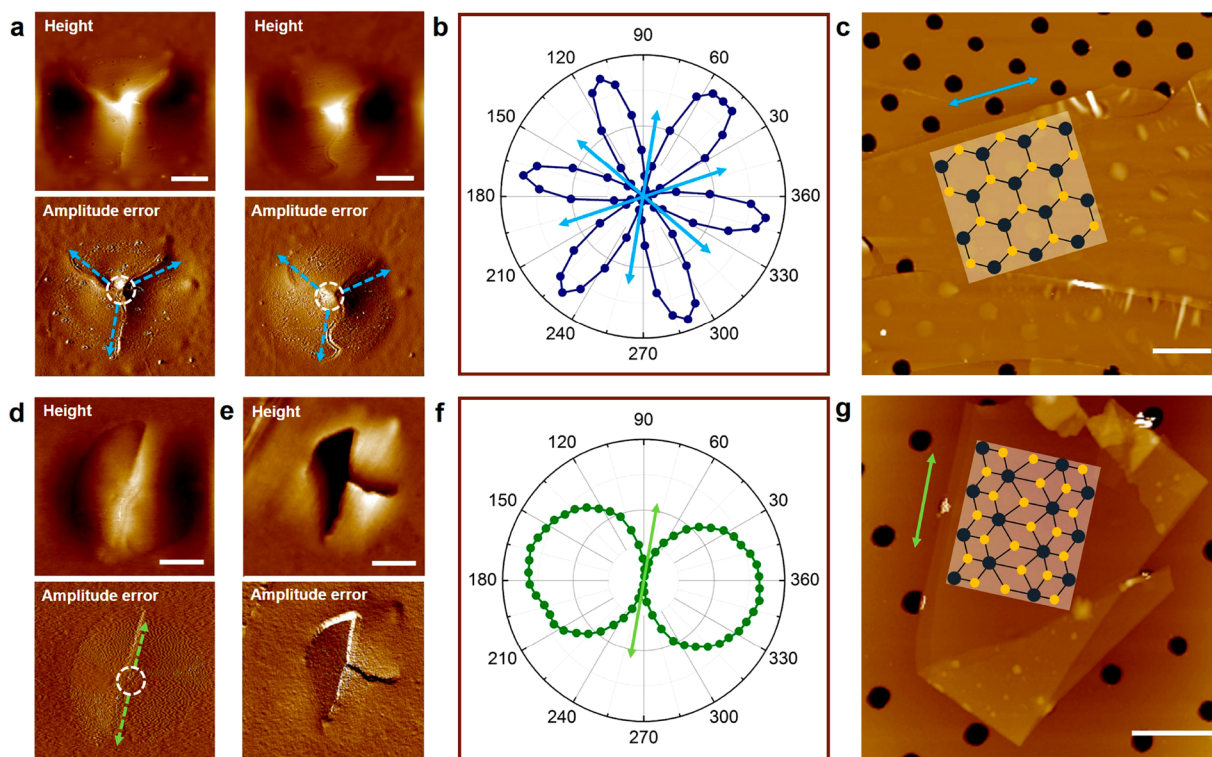


**Figure 4.** Fractures of 2H- and 1T'-MoTe<sub>2</sub>. (a) AFM images of suspended broken 2H-MoTe<sub>2</sub> membranes exhibiting Y-shaped fracture patterns. (b) SHG intensity polar map of the 2H-MoTe<sub>2</sub> flake used in panels a and c. (c) AFM image of the 2H-MoTe<sub>2</sub> flake that covers tens of holes. Inset shows its crystal structure defined by the SHG experiment. (d, e) AFM images of suspended 1T'-MoTe<sub>2</sub> membranes with linear and T-shaped fracture patterns, respectively. (f) SHG intensity polar map of the 1T'-MoTe<sub>2</sub> flake used in panels d and g. (g) AFM image of the 1T'-MoTe<sub>2</sub> flake and its crystal structure (inset). The circles in panels a and d indicate the indentation spots. The arrows in panels a–g label the directions parallel to the Mo–Mo zigzag alignment in both 2H- (cyan arrows) and 1T'-MoTe<sub>2</sub> (green arrows). Here, we use some straight edges of the samples as reference lines to align the SHG map and fracture patterns. Some straight edges of the samples are also found to be in good parallel to the Mo–Mo zigzag alignment (e.g., top edge in Figure 4c and left edge in Figure 4g). Scale bars: (a, d, e) 300 nm and (c, g) 3 μm.

insensitively on the ribbon width, giving converged results for the wide samples in experiments.

For the 2H phase,  $\Delta E_2$  of zigzag edges ( $\sim 0.569$  eV/Å) is  $\sim 12\%$  lower than that of armchair edges ( $\sim 0.645$  eV/Å), which is rationalized by the fact that the number of bonds per length along the zigzag direction is  $\sim 13\%$  smaller than that along the armchair direction. In contrast,  $\Delta E_1$  of zigzag edges becomes  $\sim 74\%$  higher than that of armchair edges after including the edge relaxation. Because the elastic energy is isotropic in the 2H phase, the preferred direction of cracks is dictated by the anisotropic  $\Delta E$  (or more specifically  $\Delta E_2$ ), which is predicted to be along the zigzag direction, consistent with our experimental results.

For the 1T' phase, both the elastic energy and  $\Delta E$  are anisotropic. Under the same strain, the elastic energy is larger along the direction having a larger elastic modulus, i.e., the armchair direction. However,  $\Delta E_2$  of zigzag edges ( $\sim 0.266$  eV/Å) is significantly lower than that of armchair edges ( $\sim 0.507$  eV/Å). The larger elastic energy along the armchair direction and the lower zigzag edge formation energy ( $\Delta E_2$ ) suggest that fracture prefers to form along the zigzag direction. Noticeably, the former value of  $\Delta E_2$  is considerably lower than that in the 2H phase. Detailed analysis found that there exists an uneven distribution of bonding strength in the reconstructed phase, and the weaker bonds (colored blue in Figure 5b) are selectively broken when forming zigzag edges, which leads to a much lower breaking strength in the 1T' phase than in the 2H phase, also in good agreement with our experiments (Table 1).

It should be noted that our DFT calculations studied fracture features of MoTe<sub>2</sub> monolayers instead of multilayers, as investigated experimentally for simplicity, based on the consideration that the interlayer vdW interactions are typically weak and play a minor role in determining fracture behavior. According to our test calculations, the relative stability of different edge shapes is essentially independent of film thickness. Thus, the theoretically predicted fracture direction is applicable for monolayer as well as multilayers, which is in agreement with our experimental observations.

In summary, by biaxial deformation of materials in nanoindentation, we have investigated the in-plane elastic moduli and breaking strengths of 2H-, 1T'-, and  $T_d$ -MoTe<sub>2</sub> as well as their fracture behaviors. The effective moduli of the three phases show little difference due to their similar atomic bonding, but the strength of the 2H phase is significantly larger than those of the 1T' and  $T_d$  phases because of the uneven distribution of bonding strengths in the latter two distorted phases. Through the direct observation of the fracture membranes together with polarization-resolved SHG, we have also deduced that the fractures prefer to propagate along the orientations of Mo–Mo zigzag chains in both isotropic and anisotropic phases, which obeys the theorem of minimum energy as revealed by the DFT calculations. Our studies provide a general approach that adopts the facile nanoindentation with biaxial deformation to probe elastic properties and fracture behaviors of structurally anisotropic

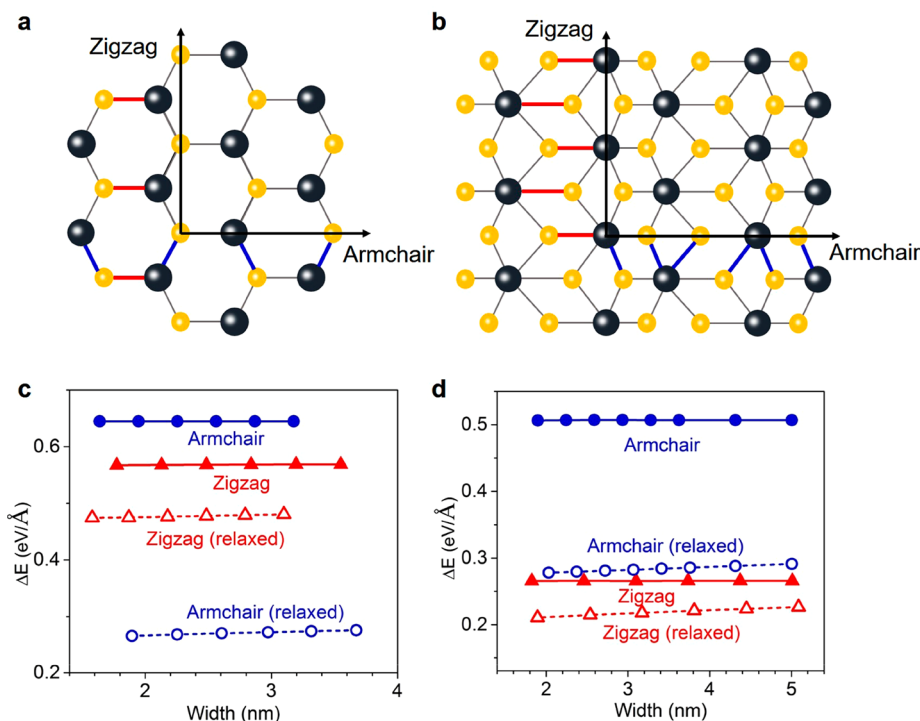


**Figure 5.** DFT calculations of edge formation energy for monolayers: (a, c) 2H- and (b, d) 1T'-MoTe<sub>2</sub>. (a, b) Armchair and zigzag edges formed by breaking blue and red bonds, respectively. (c, d) Edge formation energy per length ( $\Delta E$ ) calculated for armchair (blue circle) and zigzag (red triangle) monolayer nanoribbons with altered widths. Results excluding and including structural relaxations at the edges are represented by solid and hollow symbols, respectively.

materials, which will shed light on the development of novel flexible electronics based on versatile anisotropic 2D materials.

**Materials and Methods. Sample Preparation.** High-quality 1T'-MoTe<sub>2</sub> single crystals were grown by chemical vapor transport (CVT) using polycrystalline MoTe<sub>2</sub> as precursors. Briefly, polycrystalline MoTe<sub>2</sub> was synthesized by heating the stoichiometric mixture of high-purity Mo foil (99.95%, Alfa Aesar) and Te ingot (99.99%, Alfa Aesar) at 1073 K in a vacuum-sealed silica ampule for 3 days. The as-grown MoTe<sub>2</sub> was then recrystallized by CVT using the transporting agent, powder TeCl<sub>4</sub> (99%, Aladdin), with a concentration of  $\leq 2.7$  mg mL<sup>-1</sup>. Material transport occurred in a sealed silica ampule in a tube furnace for 3 days. After the reaction, the ampule was immediately quenched in cold water to obtain large-size 1T'-MoTe<sub>2</sub> single crystals or naturally cooled for 2H-MoTe<sub>2</sub> single crystals. MoTe<sub>2</sub> thin flakes were mechanically exfoliated onto holey substrates using a 3 M tape. The holey substrates defined with patterned circular holes (1  $\mu$ m in diameter and 285 nm in depth) were fabricated by UV photolithography and dry etching on Si wafers with a thermal oxide layer. Optical microscope (OLYMPUS BX51 M) was used to find samples of thin flakes. AFM measurement (Bruker Multimode 8, contact mode) was applied to measure the surface morphology and the layer thickness. TEM analyses (FEI Tecnai G2 F20) were applied to examine the crystal quality and the lattice structure.

**Nanoindentation.** Before indenting, a suspended membrane was scanned in tapping mode for a few times until the image became stable. Next, the scanning was paused, and the tip was indented to the center of the suspended membrane. During the indentation process, the sample stage movement,  $z$ , and the deflection of the probe,  $x$ , were simultaneously recorded. We indented each membrane with at least 5 different

forces before reaching its fracture point. After the fracture, the sample was scanned again to observe fracture pattern. The spring constant of the probe was calibrated by the Sader method (online calibration), which followed a simple harmonic oscillation model. The radius of the tip was measured by a scanning electronic microscope (Jeol 7000).

**Raman spectra and SHG measurement.** Raman spectra were measured by a Raman spectrometer (Horiba HR800) using an excitation laser with a wavelength of 532 nm. To measure Raman spectra at low temperatures, we used a cooling stage in which liquid nitrogen passed the base for cooling and nitrogen gas flowed into the chamber to avoid the formation of ice on the samples. Polarization-resolved SHG was measured using a 992 nm laser, with the average power of 5 mW. The sample was kept unmoved, and the incident laser rotates anti-clockwise. We collect one data point every 6°, with the integral time of 1 s per point.

**Raman Spectra and SHG Measurement.** Raman spectra were measured by a Raman spectrometer (Horiba HR800) using an excitation laser with a wavelength of 532 nm. To measure Raman spectra at low temperatures, we used a cooling stage in which liquid nitrogen passed the base for cooling and nitrogen gas flowed into the chamber to avoid the formation of ice on the samples. Polarization-resolved SHG was measured using a 992 nm laser, with the average power of 5 mW. The sample was kept unmoved, and the incident laser rotates anti-clockwise. We collect one data point every 6°, with the integral time of 1 s per point.

**DFT Calculations.** In our calculations of 3D bulk, a plane-wave basis set with an energy cutoff of 400 eV was used, and a  $6 \times 10 \times 2$   $\Gamma$ -point centered k-point was applied to sample the Brillouin zone. We employed a nonlocal correction function vdW-DF (optB86b)<sup>39</sup> to consider the van der Waals

interactions between neighboring MoTe<sub>2</sub> layers. The structures were fully relaxed until energy and force were converged to 10<sup>-7</sup> eV and 0.001 eV/Å, respectively. In the strain calculations, small uniaxial strains were applied along the *x* (armchair) and *y* (zigzag) directions ( $\pm 2\%$ ), and total energies were calculated and fitted with the formula  $E_s = a_1 \varepsilon_x^2 + a_2 \varepsilon_y^2 + a_3 \varepsilon_x \varepsilon_y$  using a least-squares method.<sup>11,40</sup> Here,  $E_s$ ,  $\varepsilon_x$ , and  $\varepsilon_y$  are the energy deviation from the equilibrium stage, strain along the *x* direction, and strain along the *y* direction, respectively. The 2D elastic modulus were calculated by  $E_x = (2a_1 - a_3^2/2a_1)/A_0$  and  $E_y = (2a_2 - a_3^2/2a_2)/A_0$ , where  $A_0$  is the area of the unit cell. The Poisson's ratios along the *x* and *y* axes are  $\nu_x = a_3/2a_2$  and  $\nu_y = a_3/2a_1$ , respectively. In our calculations of monolayer MoTe<sub>2</sub> and its nanoribbons, we employed the Perdew–Burke–Ernzerhof exchange correlation functional,<sup>41</sup> a plane-wave basis set with an energy cutoff of 340 eV, a vacuum layer over 15 Å together with  $17 \times 17 \times 1$  ( $9 \times 17 \times 1$ ) Monkhorst–Pack *k* points for the 2H- (1T'-) monolayer and  $9 \times 1 \times 1$  ( $17 \times 1 \times 1$ ) Monkhorst–Pack *k* points for armchair (zigzag) nanoribbons. The edge formation energy (per length) is defined as  $\Delta E = \frac{E_{nr} - E_b}{2l}$ , where  $E_{nr}$  and  $E_b$  denote the total energy of nanoribbon and its 2D monolayer bulk, respectively, and  $l$  represents the edge length.

## ■ ASSOCIATED CONTENT

### 📄 Supporting Information

The Supporting Information is available free of charge on the ACS Publications website at DOI: 10.1021/acs.nanolett.8b03833.

Details and figures regarding mechanically exfoliated samples, TEM analyses, evolution of Raman spectra, calibration of the spring constant, parameter space, typical force curve of a 2H-MoTe<sub>2</sub> sample, SEM images of the AFM probe, experimental evidence against sliding, unit cells for DFT calculations, an estimation of the force induced by sealed gas, and a calculation of the equivalent modulus (PDF)

## ■ AUTHOR INFORMATION

### Corresponding Authors

\*E-mail: yongxu@mail.tsinghua.edu.cn.

\*E-mail: qiminyan@temple.edu.

\*E-mail: liuk@tsinghua.edu.cn; phone: +86-10-62799182.

### ORCID

Liyang Jiao: 0000-0002-6576-906X

Shuyun Zhou: 0000-0002-9841-8610

Kaihui Liu: 0000-0002-8781-2495

Chun Cheng: 0000-0001-5976-3457

Wenhui Duan: 0000-0001-9685-2547

Kai Liu: 0000-0002-0638-5189

### Author Contributions

@Y.S., J.P., and Z.Z. contributed equally to this work. K.L. conceived of the project. K.Z. and Y.W. provided the MoTe<sub>2</sub> crystals. Y.S. performed the normal nanoindentation experiments. J.P. and Q.Y. calculated the elastic properties of MoTe<sub>2</sub>. Z.Z., W.D., and Y.X. calculated the fracture behaviors of MoTe<sub>2</sub>. Y.S., K.Z., and S.Z. performed the temperature-variant measurements of Raman spectra. Y.S., W.W., J.W., and C.C. performed the temperature-variant nanoindentation. J.Z. and L.J. helped with the AFM characterizations. Z.Y. and Y.H. modeled the effective modulus of anisotropic materials. Y.S.,

K.L., Q.Y., and Y.X. analyzed the data and wrote the manuscript.

### Notes

The authors declare no competing financial interest.

## ■ ACKNOWLEDGMENTS

K.L. acknowledges the support from Basic Science Center Project of NSFC under grant no. 51788104, National Key R&D Program of China (grant no. 2018YFA0208400), National Natural Science Foundation of China under grant nos. 51602173 and 11774191, Fok Ying-Tong Education Foundation under grant no. 161042, and Open Research Fund Program of the State Key Laboratory of Low-Dimensional Quantum Physics under grant no. KF201603. J.P. and Q.Y. are supported by the Center for the Computational Design of Functional Layered Materials, an Energy Frontier Research Center funded by the U.S. Department of Energy, Office of Science, Basic Energy Sciences under award no. DE-SC0012575. Part of the computational work used resources of the National Energy Research Scientific Computing Center supported by the U.S. Department of Energy under contract no. DE-AC02-05CH11231. L.J. acknowledges the support from Beijing Municipal Science & Technology Commission (no. Z161100002116030). C.C. acknowledges support from the Guangdong-Hong Kong joint innovation project (grant no. 2016A050503012).

## ■ ABBREVIATIONS

AFM, atomic force microscopy; TEM, transmission electron microscopy; SEM, scanning electron microscopy; SHG, second harmonic generation; DFT, density functional theory

## ■ REFERENCES

- (1) Desai, S. B.; Seol, G.; Kang, J. S.; Fang, H.; Battaglia, C.; Kapadia, R.; Ager, J. W.; Guo, J.; Javey, A. *Nano Lett.* **2014**, *14* (8), 4592–4597.
- (2) Fei, R.; Yang, L. *Nano Lett.* **2014**, *14* (5), 2884–2889.
- (3) Yang, S.; Wang, C.; Sahin, H.; Chen, H.; Li, Y.; Li, S. S.; Suslu, A.; Peeters, F. M.; Liu, Q.; Li, J.; Tongay, S. *Nano Lett.* **2015**, *15* (3), 1660–1666.
- (4) Sun, Y.; Wang, R.; Liu, K. *Appl. Phys. Rev.* **2017**, *4* (1), No. 011301.
- (5) Lee, C.; Wei, X.; Kysar, J. W.; Hone, J. *Science* **2008**, *321* (5887), 385–388.
- (6) Liu, K.; Yan, Q.; Chen, M.; Fan, W.; Sun, Y.; Suh, J.; Fu, D.; Lee, S.; Zhou, J.; Tongay, S.; Ji, J.; Neaton, J. B.; Wu, J. *Nano Lett.* **2014**, *14* (9), 5097–5103.
- (7) Bertolazzi, S.; Kis, A.; Brivio, J. *ACS Nano* **2011**, *5* (12), 9703–9709.
- (8) Bae, S. H.; Lee, Y.; Sharma, B. K.; Lee, H. J.; Kim, J. H.; Ahn, J. H. *Carbon* **2013**, *51*, 236–242.
- (9) Chen, C.; Rosenblatt, S.; Bolotin, K. I.; Kalb, W.; Kim, P.; Kymissis, I.; Stormer, H. L.; Heinz, T. F.; Hone, J. *Nat. Nanotechnol.* **2009**, *4* (12), 861–867.
- (10) Komaragiri, U.; Begley, M. R.; Simmonds, J. G. *J. Appl. Mech.* **2005**, *72* (2), 203–212.
- (11) Yue, Q.; Kang, J.; Shao, Z.; Zhang, X.; Chang, S.; Wang, G.; Qin, S.; Li, J. *Phys. Lett. A* **2012**, *376* (12–13), 1166–1170.
- (12) Zhang, P.; Ma, L.; Fan, F.; Zeng, Z.; Peng, C.; Loya, P. E.; Liu, Z.; Gong, Y.; Zhang, J.; Zhang, X.; Ajayan, P. M.; Zhu, T.; Lou, J. *Nat. Commun.* **2014**, *5*, 3782.
- (13) Zhang, R.; Koutsos, V.; Cheung, R. *Appl. Phys. Lett.* **2016**, *108* (4), No. 042104.
- (14) Bie, Y. Q.; Grosso, G.; Heuck, M.; Furchi, M. M.; Cao, Y.; Zheng, J.; Bunandar, D.; Navarro-Moratalla, E.; Zhou, L.; Efetov, D.

K.; Taniguchi, T.; Watanabe, K.; Kong, J.; Englund, D.; Jarillo-Herrero, P. *Nat. Nanotechnol.* **2017**, *12* (12), 1124–1129.

(15) Castellanos-Gomez, A.; van Leeuwen, R.; Buscema, M.; van der Zant, H. S.; Steele, G. A.; Venstra, W. J. *Adv. Mater.* **2013**, *25* (46), 6719–6723.

(16) Tongay, S.; Zhou, J.; Ataca, C.; Lo, K.; Matthews, T. S.; Li, J.; Grossman, J. C.; Wu, J. *Nano Lett.* **2012**, *12* (11), 5576–5580.

(17) Huo, N.; Tongay, S.; Guo, W.; Li, R.; Fan, C.; Lu, F.; Yang, J.; Li, B.; Li, Y.; Wei, Z. *Adv. Electron. Mater.* **2015**, *1* (5), 1400066.

(18) Liu, B.; Abbas, A.; Zhou, C. *Adv. Electron. Mater.* **2017**, *3* (7), 1700045.

(19) Deng, K.; Wan, G. L.; Deng, P.; Zhang, K. N.; Ding, S. J.; Wang, E. Y.; Yan, M. Z.; Huang, H. Q.; Zhang, H. Y.; Xu, Z. L.; Denlinger, J.; Fedorov, A.; Yang, H. T.; Duan, W. H.; Yao, H.; Wu, Y.; Fan, S. S.; Zhang, H. J.; Chen, X.; Zhou, S. Y. *Nat. Phys.* **2016**, *12* (12), 1105–1110.

(20) Jiang, J.; Liu, Z. K.; Sun, Y.; Yang, H. F.; Rajamathi, C. R.; Qi, Y. P.; Yang, L. X.; Chen, C.; Peng, H.; Hwang, C. C.; Sun, S. Z.; Mo, S. K.; Vobornik, I.; Fujii, J.; Parkin, S. S.; Felsner, C.; Yan, B. H.; Chen, Y. L. *Nat. Commun.* **2017**, *8*, 13973.

(21) Keum, D. H.; Cho, S.; Kim, J. H.; Choe, D. H.; Sung, H. J.; Kan, M.; Kang, H.; Hwang, J. Y.; Kim, S. W.; Yang, H.; Chang, K. J.; Lee, Y. H. *Nat. Phys.* **2015**, *11* (6), 482–488.

(22) Song, S.; Keum, D. H.; Cho, S.; Perello, D.; Kim, Y.; Lee, Y. H. *Nano Lett.* **2016**, *16* (1), 188–193.

(23) Wang, Y.; Xiao, J.; Zhu, H.; Li, Y.; Alsaied, Y.; Fong, K. Y.; Zhou, Y.; Wang, S.; Shi, W.; Wang, Y.; Zettl, A.; Reed, E. J.; Zhang, X. *Nature* **2017**, *550* (7677), 487–491.

(24) Clarke, R.; Marseglia, E.; Hughes, H. P. *Philos. Mag. B* **1978**, *38*, 121–126.

(25) Zhang, K.; Bao, C.; Gu, Q.; Ren, X.; Zhang, H.; Deng, K.; Wu, Y.; Li, Y.; Feng, J.; Zhou, S. *Nat. Commun.* **2016**, *7*, 13552.

(26) Chen, S. Y.; Goldstein, T.; Venkataraman, D.; Ramasubramanian, A.; Yan, J. *Nano Lett.* **2016**, *16* (9), 5852–5860.

(27) Tsu, R.; Hernandez, J. G. *Appl. Phys. Lett.* **1982**, *41* (11), 1016–1018.

(28) Castellanos-Gomez, A.; Poot, M.; Steele, G. A.; van der Zant, H. S.; Agrait, N.; Rubio-Bollinger, G. *Adv. Mater.* **2012**, *24* (6), 772–775.

(29) Wang, J.-Y.; Li, Y.; Zhan, Z.-Y.; Li, T.; Zhen, L.; Xu, C.-Y. *Appl. Phys. Lett.* **2016**, *108* (1), No. 013104.

(30) Lee, G. H.; Cooper, R. C.; An, S. J.; Lee, S.; van der Zande, A.; Petrone, N.; Hammerberg, A. G.; Lee, C.; Crawford, B.; Oliver, W.; Kysar, J. W.; Hone, J. *Science* **2013**, *340* (6136), 1073–1076.

(31) Rasool, H. I.; Ophus, C.; Klug, W. S.; Zettl, A.; Gimzewski, J. K. *Nat. Commun.* **2013**, *4*, 2811.

(32) Zhang, Z.; Kutana, A.; Yakobson, B. I. *Nanoscale* **2015**, *7* (6), 2716–2722.

(33) Blöchl, P. E. *Phys. Rev. B: Condens. Matter Mater. Phys.* **1994**, *50* (24), 17953.

(34) Kresse, G.; Furthmüller, J. *Phys. Rev. B: Condens. Matter Mater. Phys.* **1996**, *54* (16), 11169.

(35) Kresse, G.; Furthmüller, J. *Comput. Mater. Sci.* **1996**, *6* (1), 15–50.

(36) Li, J.; Medhekar, N. V.; Shenoy, V. B. *J. Phys. Chem. C* **2013**, *117* (30), 15842–15848.

(37) Griffith, A. A. *Philos. Trans. R. Soc., A* **1921**, *221* (582), 163–198.

(38) Beams, R.; Cancado, L. G.; Krylyuk, S.; Kalish, I.; Kalanyan, B.; Singh, A. K.; Choudhary, K.; Bruma, A.; Vora, P. M.; Tavazza, F.; Davydov, A. V.; Stranick, S. J. *ACS Nano* **2016**, *10*, 9626–9636.

(39) Klimeš, J.; Bowler, D. R.; Michaelides, A. *Phys. Rev. B: Condens. Matter Mater. Phys.* **2011**, *83* (19), 195131.

(40) Topsakal, M.; Cahangirov, S.; Ciraci, S. *Appl. Phys. Lett.* **2010**, *96* (9), No. 091912.

(41) Perdew, J. P.; Burke, K.; Ernzerhof, M. *Phys. Rev. Lett.* **1996**, *77* (18), 3865–3868.